Materials Transactions, Vol. 50, No. 9 (2009) pp. 2302 to 2307

EXPRESS REGULAR ARTICLE

Thermomagnetic Analysis of Nanocrystalline $Nd_{4.5}Fe_{77}B_{18.5}$ Alloy

Nadežda Talijan[1], Vladan Ćosović[1], Jasna Stajić-Trošić[1], Aleksandar Grujić[1], Tomáš Žák[2], Zonghoon Lee[3] and Velimir Radmilović[3]

[1]*Institute of Chemistry, Technology and Metallurgy, University of Belgrade, Belgrade 11000, Serbia*
[2]*Institute of Physics of Materials, Academy of Sciences of the Czech Rep., v.v.i., Brno CZ–616 62, Czech Republic*
[3]*National Center for Electron Microscopy, Lawrence Berkeley National Laboratory, Berkeley CA 94720-8250, USA*

Changes in the phase composition and crystallite size of a rapid quenched $Nd_{4.5}Fe_{77}B_{18.5}$ alloy, caused by thermomagnetic measurements (TM) have been studied using XRD methods of phase analysis, crystallite size and lattice microstrain determination. Structural changes in regard to optimal magnetic state were additionally analyzed by TEM. Magnetic properties in optimal magnetic state and after TM were observed using room temperature SQUID measurements. The obtained experimental results suggest the $Fe_3B/Nd_2Fe_{14}B$ and partly α-Fe nanocomposite structure of the alloy in the optimized magnetic state, with mean crystallite size (< 30 nm). After TM, an increased amount of α-Fe phase, presence of different oxide and Fe-B phases as well as growth of crystallites are found to be the main reasons for the observed quality loss of hard magnetic properties. [doi:10.2320/matertrans.M2009138]

(Received April 16, 2009; Accepted June 11, 2009; Published August 25, 2009)

Keywords: *low-neodymium neodymium-iron-boron alloy, thermomagnetic measurements, X-ray diffraction, magnetic properties*

1. Introduction

The permanent magnetic materials based on Nd-Fe-B alloys are widely used due to their outstanding magnetic properties. Alloy compositions and processing conditions have a strong influence on the microstructure of rapidly quenched Nd–Fe–B ribbons and hence on their magnetic properties. The newer nanocrystaline magnetic materials based on Nd(Pr)-Fe-B alloys with reduced Nd content, prepared by the rapid quenching method, are predominantly known as exchange-coupled nanocrystaline composite magnetic materials,[1)] having high remanence and magnetic energy despite reduced amount of expensive rare earth element (Nd). Nanocomposite permanent magnets have been recently extensively studied because of their suitability for production of bonded magnets.[2,3)] In general, the microstructure of Nd-Fe-B alloys with a low content of Nd consists of a hard magnetic phase: $Nd_2Fe_{14}B$, soft magnetic phases: α-Fe and/or Fe_3B phase and a variety of Fe-B-type phases. It is known that magnetic properties of nanocomposite Nd-Fe-B permanent magnetic materials are very sensitive to grain size and phase composition, since the exchange coupling effect is sensitive function of grain size. Increase in grain size would generally result in decrease of remanence enhancement. The main condition for obtaining a nanocomposite structure is the homogenous dispersion of a hard phase in a soft phase with a mean grain size in the nano scale (< 40 nm), because intergranular coupling between the phases only becomes more pronounced in the nano scale. The formed nanocomposites $Fe_3B/Nd_2Fe_{14}B$ and/or α-$Fe/Nd_2Fe_{14}B$ i.e. exchange interaction between mutually coupled nanocrystalline hard and soft magnetic phases are directly responsible for an increase of remanence and magnetic energy.[4)]

In this paper, the changes of phase composition and structure parameters caused by thermomagnetic measurements and their influence on magnetic behavior of the $Nd_{4.5}Fe_{77}B_{18.5}$ alloy are presented and discussed.

2. Experimental

The investigated $Nd_{4.5}Fe_{77}B_{18.5}$ alloy was produced by centrifugal atomization technique. The composition of the parental material was Nd-12 mass%, Pr-0.2 mass%, B-4.2 mass%, Al-0.3 mass%, Fe-balance. The applied quenching rate was about 25 m/s, causing a very low degree of crystallinity of the alloy in as quenched state. Previous investigations have confirmed the presence of one crystalline phase $Nd_2Fe_{14}B$, while the presence of NdO_2 and Fe_3B crystalline phases could not be excluded.[5)] The as quenched powder was subsequently annealed at 660°C for 5 min. The applied heat treatment regime was optimized in preceding investigations.[6–8)] Its basic magnetic characteristics in the optimized magnetic state were ${}_iH_c = 0.22$ MA/m, $B_r = 1.09$ T and $(BH)_{max} = 85.1$ kJ/m^3.

Thermomagnetic (TM) analysis was performed in the temperature interval 20–800°C using a vibrating sample magnetometer in a field of intensity of 4 kA/m under low vacuum. The powder of investigated alloy was cold-pressed into small tablets having diameter of about 3 mm. The samples were heated up to 800°C with heating and cooling rate kept at 4°C/min.

In order to investigate the changes in structure and phase composition that have direct influence on magnetic properties, caused by TM, corresponding microstructural analyses and magnetic measurements were carried out before (in optimized magnetic state) and after the TM.

Phase composition and crystallite size of the rapid-quenched Nd-Fe-B alloy were determined by X-Ray powder diffraction (XRD) analysis. For the XRD data collection a Philips_Xcelerator automated X-ray powder diffractometer was used. The diffractometer was equipped with a Co-tube. The generator was set-up on 40 kV and 30 mA. A fixed divergence slit 0.76 mm was used. Data for the Rietveld refinement were collected in a continuous mode between 20 and 110° 2θ. Intensity was averaged at every 0.002° 2θ.

The X-ray line-broadenings were analyzed by Fullprof software.[9] In the Fullprof program, X-ray line broadenings were analyzed through refinement of the Thompson Cox Hastings-pseudo Voight (TCH-pV) function parameters, in this case most reliable peak-shape function. For the instrumental broadening correction, standard specimen LaB_6 was used. XRPD pattern of the standard was fitted by convolution to the experimental TCH-pV ($U = 0.002815$; $V = -0.003345$; $W = 0.001761$; $X = 0.000076$; $Y = 0.040512$ for CoKα_1 and $U = 0.006021$; $V = -0.004091$; $W = 0.001481$; $X = 0.000076$; $Y = 0.040512$ for CoKα_2). Average values of the apparent size and mixing strain are averaged over all directions in the reciprocal space. Values in the parentheses measure degree of anisotropy of the apparent size and maximal strain. Details of the applied models could be found elsewhere.[9]

Quantitative phase analysis was done by the FullProf[9] computer program. For quantitative analysis sample was carefully prepared to comply with the definition of a "powder": homogeneity and sufficient number of particles with random orientation. According to Brindley[10] and Hill & Howard,[11] in a mixture of N crystalline phases the weight fraction W_j of phase j is given by:

$$W_j = \frac{(S_j Z_j M_j V_j)/\tau_j}{\sum_i (S_i Z_i M_i V_i)/\tau_i} \quad (1)$$

where: S_j is the scale factor of phase j, Z_j is the number of formula units per unit cell for phase j, M_j is the mass of the formula unit, V_j is the unit cell volume, τ_j is the Brindley particle absorption contrast factor for phase j defined as:

$$\tau_j = \frac{1}{V_j} \int \exp\{-(\mu_j - \mu_u)x\} dV_j \quad (2)$$

where: V_j is the volume of a particle of phase j, μ_j is the particle linear absorption coefficient, μ_u is the mean linear absorption coefficient of the solid material of the powder, x is the path of the radiation in the particle of phase j when reflected by the volume element dV_j. The latter parameter accounts for microabsorption effects that become important when the compounds of the powder have rather different linear absorption coefficients. Its calculation requires only the knowledge of the particle radius and linear absorption coefficient μ. We have assumed that particle radius for all phase was 15 µm.

Further microstructural analysis was performed on JEOL JEM 200CX transmission electron microscope (TEM). The samples for TEM analysis were prepared using focused ion beam microscopy (FIB). Magnetic properties of alloy i.e. corresponding hysteresis loops were obtained at ambient temperature using Quantum Design MPMS 5XL Superconducting Quantum Interference Device (SQUID) magnetometer with magnetic field strength in range −3.98 to 3.98 MA/m.

3. Results and Discussion

The thermomagnetic behavior of the rapid quenched $Nd_{4.5}Fe_{77}B_{18.5}$ alloy and the corresponding phase transformations were analyzed by TM. The obtained TM curves, presented in Fig. 1, illustrate themomagnetnic properties and phase composition of the investigated alloy.

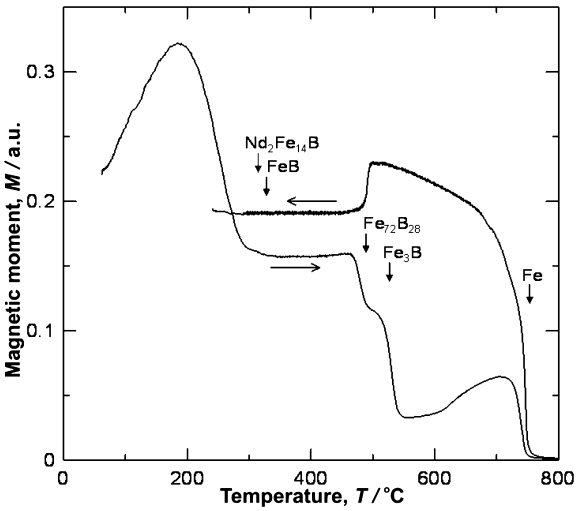

Fig. 1 TM curves of the $Nd_{4.5}Fe_{77}B_{18.5}$ alloy.

Next applied method of analysis that provides information about phase composition and microstructure in general i.e. explains the constitution of some minor phases and validates presence of others is XRD. The obtained diffraction spectra confirmed the complexity of both materials (see Fig. 2).

In the optimized magnetic state of the alloy, Fe_3B, $Nd_2Fe_{14}B$, α-Fe and Fe-B phases were identified by XRD analysis. The presence of a $Fe_{72}B_{28}$ phase,[12] illustrated on TM curves (Fig. 1), is to be understood more as a representative of Fe(Nd,B) and Fe(B) components, which most likely have origin on surfaces and/or interfaces of fine grains of individual phases, as determined by ^{57}Fe Mössbauer spectroscopic analysis published in Ref. 5). On the presented XRD spectra (Fig. 2) atoms of such structures probably appear just in the form of an elevated background count. Although the compositional studies on the phases of the Nd-Fe-B alloys with a low content of Nd show that the formation of metastable $Nd_2F_{23}B_3$ phase can be expected,[13–15] XRD analysis was not able to confirm its presence in the alloy after the optimal heat treatment. It could be that this phase is present in very small quantities that are below the sensitivity threshold or that the heating rate during the annealing was high enough to avoid the formation of this intermediate metastable phase, as reported by Gao *et al.*[16]

According to the results of XRD analysis (Fig. 2), phase composition of the investigated alloy in the state after the TM (20–800°C) is characterized by presence of larger number of soft and paramagnetic phases. The main hard magnetic $Nd_2Fe_{14}B$ phase is accompanied by α-Fe, Fe_3B phases and a number of different Fe-B phases, as well as a boride phase $Nd_{1.1}Fe_4B_4$. The appearance of non-ferromagnetic boron rich $Nd_{1.1}Fe_4B_4$ phase, can be explained as a consequence of high boron content in the investigated alloys (above 4.2 at%).[13] It was found that $Nd_{1.1}Fe_4B_4$ phase forms in non-uniformly distributed heavily faulted grains of approximately the same dimensions as grains of $Nd_2Fe_{14}B$ phase.[17] Since its Curie temperature is very low (Tc = 13 K), the $Nd_{1.1}Fe_4B_4$ phase does not exhibit ferromagnetic behavior at room temperature environment and consequently

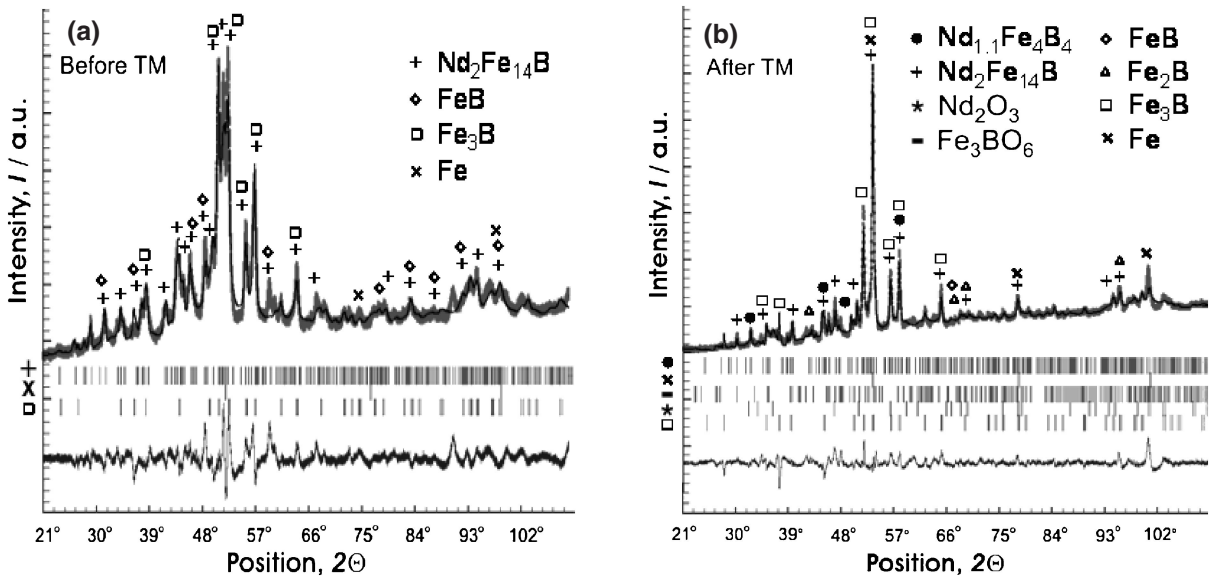

Fig. 2 XRD diffractograms of the $Nd_{4.5}Fe_{77}B_{18.5}$ alloy with comparison of observed and calculated intensities: (a) before TM, (b) after TM.

Table 1 Unit cell parameters, Brindley factors, size-strain parameters and R-factors for the $Nd_{4.5}Fe_{77}B_{18.5}$ alloy before TM.

	$Nd_2Fe_{14}B$		**α-Fe**		**Fe_3B**	
	refined	literature data[19]	refined	literature data[20]	refined*	Ni_3P literature data[21]
a/Å	8.7537(4)	8.803(1)	2.89457(7)	2.8665(2)	8.6213(5)	8.954(4)
b/Å	8.7537(4)	8.803(1)	2.89457(7)	2.8665(2)	8.6213(5)	8.954(4)
c/Å	12.194(1)	12.196(1)	2.89457(7)	2.8665(2)	4.2992(7)	4.386(2)
α	90°	90°	90°	90°	90°	90°
β	90°	90°	90°	90°	90°	90°
γ	90°	90°	90°	90°	90°	90°
Volume, V/Å^3	934.4	945.1	24.25	23.55	319.5	351.6
Bridnley factor, τ	0.865	—	1.012	—	1.012	—
Mass percentage (%)	43.6(3)	—	16.5(3)	—	39.8(3)	—
Average appar. size, $\langle D \rangle$/Å	120.0(2)	—	54.34(1)	—	248.0(2)	—
Average max. strain $\times 10^4$, $\langle \varepsilon \rangle$	18.09(4)	—	18.087(1)	—	16.87(1)	—
R-factors not corrected for background						
R_{wp}	2.80	—	2.80	—	2.80	—
R_p	1.99	—	1.99	—	1.99	—
χ^2	13.7	—	13.7	—	13.7	—
Conventional Rietveld R-factors						
R_{wp}	20.9	—	20.9	—	20.9	—
R_p	23.0	—	23.0	—	23.0	—
χ^2	13.7	—	13.7	—	13.7	—

*unit cell parameters from PDF # 39-1315[22] (a = 8.673 Å, b = 8.673 Å, c = 4.312 Å, $\alpha = 90°$, $\beta = 90°$, $\gamma = 90°$, V = 324.46 Å^3) are in reasonable agreement with the refined.

it is deleterious to the magnetic properties of the magnets.[18] Still, small amounts of this phase can be quite commonly found in Nd-Fe-B magnetic materials. The presence of the Nd_2O_3 phase and other oxide phases formed during the TM can be also observed.

To obtain a better understanding of the influence of phase composition and crystallite size of the identified phases on the magnetic properties before and after TM, size-strain and quantitative phase analyses of the XRD data were performed. The amount of the hard and soft magnetic phases and their crystallite sizes, calculated by Full-Prof program are presented in Table 1 and Table 2. Comparisons between observed and calculated intensities are presented in Fig. 2. The vertical bars indicate the

Table 2 Unit cell parameters, Brindley factors, size-strain parameters and R-factors for the $Nd_{4.5}Fe_{77}B_{18.5}$ alloy after TM.

	$Nd_2Fe_{14}B$		**α-Fe**		**Fe_3B**		**Nd_2O_3**		**Fe_3BO_6**	
	refined	literature data[19]	refined	literature data[20]	refined#	Ni_3P literature data[21]	refined*	literature data[23]	refined	literature data[24]
a/Å	8.7743(5)	8.803(1)	2.86825(9)	2.8665(2)	8.6082(4)	8.954(4)	3.851(2)	3.831	9.36(1)	10.048(2)
b/Å	8.7743(5)	8.803(1)	2.86825(9)	2.8665(2)	8.6082(4)	8.954(4)	3.851(2)	3.831	7.889(7)	8.531(2)
c/Å	12.165(1)	12.196(1)	2.86825(9)	2.8665(2)	4.3000(4)	4.386(2)	6.371(4)	5.999	5.469(9)	4.466(1)
α	90°	90°	90°	90°	90°	90°	90°	90°	90°	90°
β	90°	90°	90°	90°	90°	90°	90°	90°	90°	90°
γ	90°	90°	90°	90°	90°	90°	120°	120°	90°	90°
Volume, V/Å^3	936.6	945.1	23.60	23.55	318.63	351.6	81.83	76.25	404.0	382.8
Bridnley factor, τ	0.840	—	1.008	—	1.008	—	0.460	—	1.011	—
Mass percent (%)	17.95(6)	—	36.8(6)	—	28.2(6)	—	8.0(6)	—	9(1)	—
Average appar. size, $\langle D \rangle$ /Å	385.7(8)	—	289.8(1)	—	337.4(4)	—	79.04()	—	112.9(1)	—
Average max. strain $\times 10^4$, $\langle \varepsilon \rangle$	3.171(5)	—	3.1709(8)	—	3.171(4)	—	3.171(1)	—	3.171(5)	—
R-factors not corrected for background										
R_{wp}	3.50	—	3.50	—	3.50	—	3.50	—	3.50	—
R_p	2.30	—	2.30	—	2.30	—	2.30	—	2.30	—
χ^2	13.2	—	13.2	—	13.2	—	13.2	—	13.2	—
Conventional Rietveld R-factors										
R_{wp}	25.3	—	25.3	—	25.3	—	25.3	—	25.3	—
R_p	30.4	—	30.4	—	30.4	—	30.4	—	30.4	—
χ^2	13.2	—	13.2	—	13.2	—		—		—

*probably transformed to the high-temperature disordered Nd_2O_3 phase[25] (a = 3.912(3) Å, b = 3.912(3) Å, c = 6.227(4) Å, $\alpha = 90°$, $\beta = 90°$, $\gamma = 120°$, V = 82.53 Å^3).

#unit cell parameters from PDF # 39-1315[22] (a = 8.673 Å, b = 8.673 Å, c = 4.312 Å, $\alpha = 90°$, $\beta = 90°$, $\gamma = 90°$, V = 324.46 Å^3) are in reasonable agreement with the refined.

positions of the reflections and the difference patterns are given below.

Different ability of phases to absorb X-rays was taken into account for the calculation of content of crystalline phases. The results of XRD show very good agreement with the results of chemical analysis. For the sample in the state before TM, mass amounts of each cation (per gram of the sample) calculated from the phase mass percentages are: Nd-11.64%, Fe-85.51%, B-2.85%. After the TM individual atom mass contents are: Nd-11.66%, Fe-81.76%, B-2.24%, O-4.41%. When judging the validity of the obtained agreement, partial oxidation of the sample after the TM should be considered. Furthermore, a rather good correspondence of the individual atom content in the sample before and after the TM can be observed as well.

Unit cell of the $Nd_2Fe_{14}B$ phase in the state before and after TM (Table 1, Table 2) is slightly smaller compared to the values found in literature, which can be caused by embedding of the Pr atom in crystal structure. Somewhat bigger unit cell of α-Fe phase before the TM is probably the consequence of embedding of Nd (or even Pr) atom in the α-Fe structure. On the other side, after the TM Nd (and maybe Pr) atoms most likely "leave" the α-Fe structure.

After the TM, slightly bigger unit cell of Nd_2O_3 than theoretical can be observed (Table 2). This is possibly the consequence of the transformation of the microstructure into high temperature disordered state.[25] Bigger unit cell of Fe_3BO_6 is probably caused by embedding of the Nd (or Pr) atoms in the structure which could replace Fe atoms, as well as possible replacement of B atom with Al atom.

In the both samples, before and after TM, Pr atoms are most probably replacing Nd atoms in the Nd-containing phases. However, Al atoms were not detected, so it is possible that Al atoms are replacing Fe atoms in Fe-containing phases or that they are included in some remnant amorphous phase.

Results of microstructural analysis of the material in the state before TM show low degree of crystallinity of the present phases, in particular α-Fe. Small sizes of crystallites and high values of microstrain support this. Microstructural

analysis also demonstrates that the phases that are present in the material after the TM have different degree of crystallinity i.e. different number of defects in microstructure. Due to complexity of diffractogram, all phases have averaged equal values of microstrain. Comparison of values of microstructural parameters of $Nd_2Fe_{14}B$ and α-Fe phases before and after TM suggests that these phases have greater crystallinity after the TM i.e. smaller number of defects.

From the results of XRD analysis (Fig. 2, Table 1 and Table 2), it is obvious that after TM, the amount of main hard magnetic phase $Nd_2Fe_{14}B$ decreases in respect to the optimized magnetic state. Consequently, the number and content of soft magnetic phases had increased, predominantly α-Fe. The average crystallite size of all identified phases had also increased. Practically, the increase of temperature during TM resulted in thermal decomposition of the alloy and growth of the crystallites. Moreover, partial oxidation of the alloy during the TM can be observed, as the presence of Nd_2O_3 and Fe_3BO_6 phases was determined.

The bright field TEM micrograph (Fig. 3(a)), showing the average grain size in the optimized magnetic state below 30 nm, confirms the mean crystallite size calculated from the XRD data. Thus, on average, this indicates that one grain is composed of one crystallite. A microdiffraction analysis gave evidence for the mixing of the nanocrystalline phases. Taken together the results of XRD and TEM analyses imply that the alloy in optimized state has a nanocomposite structure of $Fe_3B/Nd_2Fe_{14}B$ type and partly α-Fe. TEM analysis of the sample after TM has confirmed the growth of the crystallites induced by increase of temperature up to 800°C (Table 2, Fig. 3(b)). The obtained electron diffraction patterns show very high density of diffraction rings, due to which the reliable identification of present phases was not possible.[26)]

The shape of corresponding SQUID hysteresis loops (Fig. 4) demonstrate the considerable difference between the state with optimized magnetic properties and the state after the thermal decomposition induced by the TM.

The hysteresis loop for the optimized magnetic state (Fig 4(a)) indicates the presence of the interaction of ferromagnetic exchange coupling between the grains of hard magnetic $Nd_2Fe_{14}B$ phase and soft magnetic phases, suggesting the nanocomposite structure of the investigated alloy. The obtained high value of remanence ($B_r = 1.09$ T) and calculated remanence ratio ($Jr/Js = 0.6$), higher than the theoretical limit for an assembly of isotropic non-interacting single domain particles given by the Stoner-Wohlfarth theory,[27)] support this. The change of magnetic behavior after the TM, which is clearly visible in Fig. 4(b), is in correspondence with the phase transformations and structural changes which have occurred during the TM. Increased amount of the main decomposition product α-Fe and presence of a number of different Fe-B and oxide phases as well as increase of mean grain size after the TM are the main reason for the quality loss of investigated magnetic material.

4. Conclusion

The presented experimental results clearly illustrate the substantial difference in the structure, phase composition and corresponding magnetic properties of the rapid-quenched

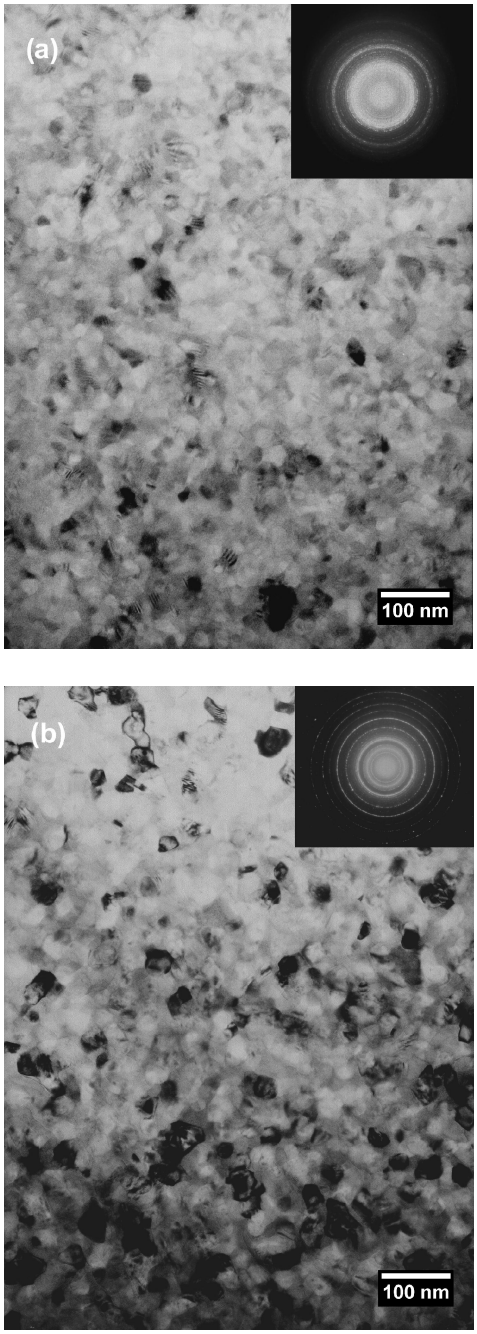

Fig. 3 Bright field TEM micrographs of the $Nd_{4.5}Fe_{77}B_{18.5}$ alloy: (a) optimized state; (b) after TM.

$Nd_{4.5}Fe_{77}B_{18.5}$ alloy in optimized magnetic state and in state after thermomagnetic measurements. Both the mean crystallite size and grain size of the investigated alloy in optimal magnetic state determined by XRD and TEM analysis were below 30 nm indicating that in average one grain is composed of one crystallite i.e. all crystalline phases were well crystallized. Composed of $Nd_2Fe_{14}B$, Fe_3B and α-Fe phases, the alloy in the optimized magnetic state has mainly a nanocomposite structure. The value of the remanent ratio $Jr/Js > 0.5$, calculated from the SQUID hysteresis loop, suggests that exchange coupling interactions between grains of the soft and hard magnetic phase exist. This assumption is supported by the higher value of the remanence and $(BH)_{max}$, which are typical for nanocomposite structures of Nd-Fe-B

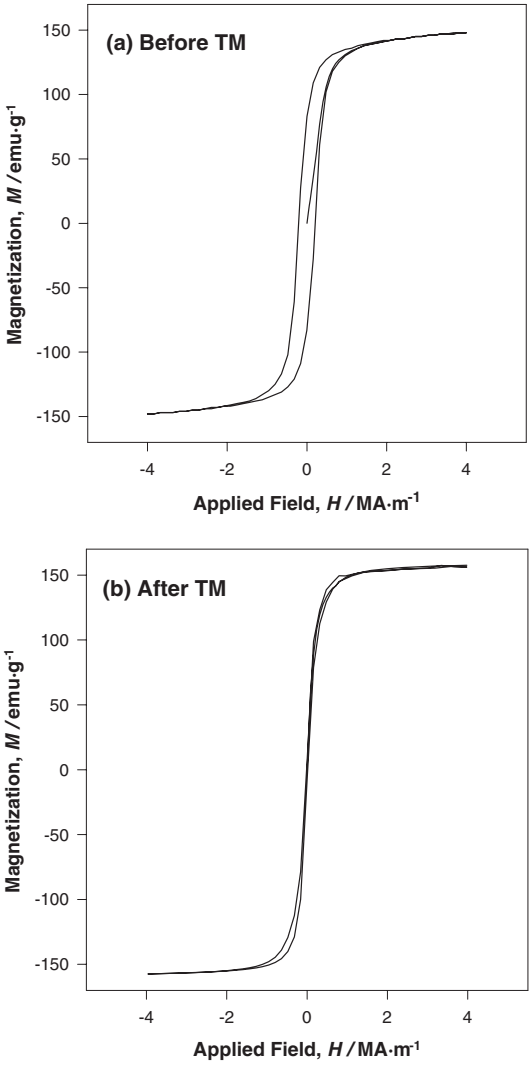

Fig. 4 Hysteresis loops of the rapid quenched $Nd_{4.5}Fe_{77}B_{18.5}$ alloy: (a) optimized magnetic state; (b) after TM.

alloys. The increase of temperature during TM resulted in the growth of the crystallites and a decrease of the amount of $Nd_2Fe_{14}B$, due to an increase in the amounts of the α-Fe and Nd-oxide fractions, in respect to the optimized magnetic state.

Altogether, the results of XRD, TEM analyses and SQUID magnetic measurements show that the structural and microstructural changes (phase compositions, crystallite size) have a direct influence on magnetic behaviour and they are the main reason for the deterioration of magnetic properties after the thermomagnetic measurements.

Acknowledgement

This work has been supported by the Serbian Ministry of Science, project OI 142035B and by the Czech Ministry of education, youth and sports, project 1M0512. The authors acknowledge support of the National Center for Electron Microscopy, Lawrence Berkeley Lab, which is supported by the U.S. Department of Energy under Contract # DE-AC02-05CH11231.

REFERENCES

1) R. Coehoorn, D. B. de Mooij, J. P. W. Duchateau and K. H. J. Buschow: J. de Phys. **49** (1988) C8-669-670.
2) D. H. Ping, K. Hono, H. Kanekiyo and S. Hirosawa: Acta Mater. **47** (1999) 4641–4651.
3) A. Manaf, R. A. Buckley, H. A. Davies and M. Leonowicz: J. Magn. Magn. Mater. **101** (1991) 360–362.
4) H. Kanekiyo, M. Uehara and S. Hirosawa: IEEE Trans. Magn. **MAG-29** (1993) 2863–2865.
5) V. Ćosović, T. Žák, N. Talijan, A. Grujić and J. Stajić-Trošić: J. Alloy. Compd. **456** (2008) 251–256.
6) N. Talijan, T. Žák, J. Stajić-Trošić and V. Menushenkov: J. Magn. Magn. Mater. **258–259** (2003) 577–579.
7) V. Ćosović, A. Grujić, J. Stajić-Trošić, V. Spasojević and N. Talijan: Mat. Sci. Forum **555** (2007) 527–532.
8) A. Grujić, V. Ćosović, J. Stajić-Trošić, A. Maričić and N. Talijan: Sci. Sint. **39** (2007) 193–198.
9) R.-Carvajal: J. FullProf.2k (Version 2.40-May 2003-LLB JRC) Computer program; www-llb.cea.fr/fullweb/fp2k/fp2k.htm.
10) G. W. Brindley: Phil. Mag. **36** (1945) 347–369.
11) R. J. Hill and C. J. Howard: J. Appl. Cryst. **20** (1987) 467–476.
12) C. L. Chien, D. Musser, E. M. Gyorgy, R. C. Sherwood, H. S. Chen, F. E. Luborsky and J. L. Walter: Phys. Rev. B **20** (1979) 283–295.
13) R. Coehoorn, D. B. de Mooij and C. de Waard: J. Magn. Magn. Mater. **80** (1989) 101–104.
14) K. H. J. Buschow, D. B. De Mooij and R. Coehoon: J. Less-Common Met. **145** (1988) 601–611.
15) Y. Q. Wu, D. H. Ping, B. S. Murty, H. Kanekiyo, S. Hirosawa and K. Hono: Scr. Mater. **45** (2001) 355–362.
16) Y. Gao, S. Zhang and B. Liu: J. Magn. Magn. Mater. **208** (2000) 158–162.
17) X. J. Yin, H. E. Evan, I. R. Harris and I. P. Jones: Oxidation of Metals **59** (2003) 167–182.
18) S. C. Wang and Y. Li: J. Mat. Sci. **40** (2005) 3853–3855.
19) J. F. Herbst, J. J. Croat and W. B. Yelon: J. Appl. Phys. **57** (1984) 4086–4090.
20) E. A. Owen and E. L. Yates: J. Chem. Phys. **3** (1935) 605–616.
21) E. Larsson: Arkiv foer Kemi ARKEA **23** (1965) 335–365.
22) Y. Z. Khan, E. Kneller and M. Sostarich: Z. Metallk. **73** (1982) 624.
23) J. X. Boucherle and J. Schweizer: Phase Trans. **38** (1992) 127–220.
24) R. Diehl and G. Brandt: Acta Cryst. B **31** (1975) 1662–1665.
25) P. Aldebert and J. P. Traverse: Mater. Res. Bull. **14** (1979) 303–323.
26) V. Ćosović: PhD thesis, (TMF-University of Belgrade, 2008).
27) E. F. Kneller and R. Hawig: IEEE Trans. Magn. **27** (1991) 3588–3600.